Spatial changes in the atrial fibrillation wave-dynamics after using antiarrhythmic drugs: A computational modeling study

Directed by Professor Hui-Nam Pak

The Master's Thesis
submitted to the Department of Medical Science
the Graduate School of Yonsei University
in partial fulfillment of the requirements for the degree of
Master of Medical Science

Inseok Hwang

December 2021

This certifies that the Master's Thesis of
Inseok Hwang is approved.

- ----------

Thesis Supervisor : Hui-Nam Pak

- ----------

Thesis Committee Member#1 : Hee Tae Yu

- ----------

Thesis Committee Member#2 : Hangsik Shin

The Graduate School
Yonsei University

December 2021

ACKNOWLEDGEMENTS

I would like to express my gratitude to Professor Hui-Nam Pak, who taught me not just how to become a better researcher but also how to become a better person during the course of my degree. Also, I would like to express my gratitude to Dr. Byounghyun Lim, Dr. Myunghee Hong, and Dr. Oh-Seok Kwon. Also, I would like to take this opportunity to express my gratitude to Song-Yi Yang, Hee-Jin Han, Seonkyu Kim, Jisu Lee, So-Hyun Yang, and Dr. Je Jin. I would also like to send my gratitude to Professor Hee Tae Yu and Professor Hangsik Shin for all the help throughout the course of my degree. I will do our best to become a researcher who can contribute to society by further developing research. I would like to thank Mr. John Martin for his linguistic assistance.

<TABLE OF CONTENTS>

ABSTRACT ····· 1
I. INTRODUCTION ····· 3
II. MATERIALS AND METHODS ····· 5
1. Ethical approval ····· 5
2. Activation Time Matching ····· 5
3. Virtual AAD intervention ····· 9
4. AF Induction, dominant frequency, and Smax analyses ····· 14
5. Statistical analyses ····· 18
III. RESULTS ····· 19
1. Effects of AADs on the AF wave-dynamics ····· 19
2. Different AAD effects on the PV and extra-PV regions ····· 24
3. Post-AAD mean DF depending on the Smax ····· 26
4. Termination or defragmentation of AF depending on the DF and COV-DF ····· 31
IV. DISCUSSION ····· 35
1. Main findings ····· 35
2. Anti-AF effects of AADs on the PV or extra-PV regions ····· 35
3. AF mechanisms of multiple wavelets or focal sources ····· 36
4. Sufficient conditions for AF defragmentation or termination ····· 37
5. Limitations ····· 38
V. CONCLUSION ····· 40
REFERENCES ····· 41
ABSTRACT (IN KOREAN) ····· 46

LIST OF FIGURES

Figure 1. Computational modeling of the left atrium with AF · 8
Figure 2. Pacing and recording location of electrogram ····· 15
Figure 3. Overall 3D DF maps and high DF areas ····· 16
Figure 4. Overall 3D Smax, and high Smax areas ····· 17
Figure 5. The effects of AADs on extra-PV and PV regions ··· 21
Figure 6. Changes in the DF during a high and low Smax ····· 28
Figure 7. Changes in the DF during Termination and Atrial Tachycardia····· 34
Figure 8. Heterogeneity of DF ····· 34

LIST OF TABLES

Table 1. AAD Ion currents for Courtemanche Ramirez Nattel model ····· 10
Table 2. References for atrial cell ion currents depending on AADs ····· 12
Table 3. Baseline characteristics ····· 20
Table 4. Effects of AADs on the electrophysiological and fibrillatory wave-dynamics parameters ····· 22
Table 5. Effects of AADs on the PV vs. Extra-PV tissue ····· 25
Table 6. AF wave-dynamics depending on the Smax values ··· 27
Table 7. AF wave-dynamics depending on the Smax values with AADs ····· 29
Table 8. Electrophysiological characteristics terminated AF after AADs ····· 32

ABSTRACT

Spatial changes in the atrial fibrillation wave-dynamics after using antiarrhythmic drugs: A computational modeling study

Inseok Hwang

Department of Medical Science
The Graduate School, Yonsei University

(Directed by Professor Hui-Nam Pak)

Background We previously reported that a computational modeling-guided anti-arrhythmic drug (AAD) test was feasible for evaluating multiple AADs in patients with atrial fibrillation (AF). We explored the anti-AF mechanisms of AADs and spatial change in the AF wave-dynamics by a realistic computational model.

Methods We used realistic computational modeling of 25 AF patients (68% male, 59.8±9.8 years old, 32.0% paroxysmal AF) reflecting the anatomy, histology, and electrophysiology of the left atrium (LA) to characterize the effects of 5 AADs (amiodarone, sotalol, dronedarone, flecainide, and propafenone). We evaluated the spatial change in the AF wave-dynamics by measuring the mean dominant frequency (DF) and its coefficient of variation (DF-COV) in 10 segments of the LA. The mean DF and DF-COV were compared according to the pulmonary vein (PV) vs. extra-PV, maximal slope of the restitution curves (Smax), and defragmentation of AF.

Results The mean DF decreased after the administration of AADs in the dose dependent manner ($p<0.001$). Under AADs, the DF was significantly lower ($p<0.001$) and COV-DF higher ($p=0.003$) in the PV than extra-PV region. The mean DF was

significantly lower at a high Smax (≥1.4) than a lower Smax condition under AADs. During the episodes of AF defragmentation, the mean DF was lower ($p<0.001$), but the COV-DF was higher ($p<0.001$) than that in those without defragmentation.

Conclusions The DF reduction with AADs is predominant in the PVs and during a high Smax condition and causes AF termination or defragmentation during a lower DF and spatially unstable (higher DF-COV) condition.

Key words: Atrial fibrillation, Computational modeling, Antiarrhythmic drug, Dominant frequency, Spatial changes

Spatial changes in the atrial fibrillation wave-dynamics after using antiarrhythmic drugs: A computational modeling study

Inseok Hwang

Department of Medicine Science
The Graduate School, Yonsei University

(Directed by Professor Hui-Nam Pak)

I. INTRODUCTION

Atrial fibrillation (AF) is a common arrhythmia, with a prevalence of more than 1.6% of the total population, and the prevalence continues to increase in the aging society [1]. Antiarrhythmic drugs (AADs) are the most commonly used first-line treatment for AF rhythm control. However, inadvertent use of AADs can increase the mortality [2,3] and has the risk of various side effects [4]. After the establishment of the guidelines of AF management on the use of AADs, the safety of AADs has been improving, and early rhythm control using AADs ensures a better prognosis in AF patients [5,6]. Nevertheless, as AADs are ion channel blockers, their efficacy highly varies from person to person due to the interaction of multiple ion channels and the genetic influence [7] and remains unsatisfactory [8]. Many experimental studies have conducted to investigate the effects of AADs, however, most of the studies were results of animal studies [9]. Previous study indicated that APD heterogeneity promoted substrate for arrhythmogenic re-entrant waves during AF initiation and maintenance. Amiodarone has shown anti-AF effect by increasing atrial APD and reducing APD heterogeneity. Increasing atrial APD and reduced APD heterogeneity were effective in controlling

arrhythmogenic reentry [9]. If the rhythm control effect of AADs can be predicted through simulation modeling, an efficient selection of AADs might be possible and can reduce the adverse effects or trial and error. We recently reported that the virtual AAD test can be performed through computational modeling reflecting the personalized atrial anatomy, histology, and electrophysiology of AF patients [10]. Computational modeling can evaluate the efficacy of multiple AADs under the same condition and can quantify the mechanistic effects of AADs using very high-spatiotemporal resolution maps [10-14]. This virtual AAD test does not have any ethical problems because it allows testing of multiple drugs with variable doses without the risk of adverse events [10]. This study analyzed the mechanism of the AAD effects on the AF wave-dynamics using an AF computational modeling that reflected the anatomical, histological, and electrophysiological characteristics of 25 patients with AF. The purpose of this study was to quantify the dominant frequency (DF) and its spatial heterogeneity after using AADs [12,15,16] and to compare the regional differences between the pulmonary veins (PVs) and extra-PV regions and differences according to the AF wave-break conditions [12]. In addition, we compared the characteristics of the wave-dynamics in episodes of AF termination or defragmentation under AAD use.

II. MATERIALS AND METHODS

1 Ethical approval

The study protocol followed the Declaration of Helsinki and was approved by the Institutional Review Board of the Severance Cardiovascular Hospital, Yonsei University Health System. All participants were included in Yonsei AF Ablation Cohort Database (ClinicalTrials.gov Identifier: NCT02138695) and provided written consent to participate in the study.

2 Activation Time Matching

First, electroanatomical modeling using patient voltage data was conducted. Over 500 bipolar voltage data points that included sequential recordings of electrograms at a 500 ms cycle length were obtained from the surface of the individual atria during AF catheter ablation (Figure 1). The individual CT images were merged with the voltage data to produce the personalized electroanatomical environment of each patient. The inverse distance weighting (IDW) method [17] was used to interpolate the clinical voltage signal for a simulation. The interpolation was based on the inverse distance weighting method (IDW) [17] and was within a 10-mm radius from the region of interest. Interpolation of the clinical voltage data produced a virtual voltage map with an amplitude. The detailed equation for the IDW was as follows:

$$W_{ij} = \frac{{d_{ij}}^{-a}}{\sum_k^{n_j} d_{k_j}},\ R_j = \sum_{i=1}^{n_j} w_{ij} R_{ij}$$

where W demonstrated the weighted average of neighboring values; i and j

represented the unknown and known values of the respective points; d_{ij}^{-a} was the distance between unknown and known points; R_j represented the interpolation value at unknown point j; and R_{ij} indicated the known point of the value. The 3D LA model was created using the interpolated voltage map and CT images through the Ensite Navx system (Abbott Inc., Lake Bluff, IL, USA). Accurate matching of the voltage and CT images data on the 3D LA model was conducted using rotation and translation. We interpolated a clinical voltage map to produce a virtual voltage map on 3D model. The registration of the electro-anatomical maps onto the CT models involved the four following steps: geometry, trimming, field scaling, and alignment. The registration error could occur during such steps. Each step was conducted manually by an operator therefore possible human error potentially existed [18]. The fiber orientation involved two states: tracking and visualization. Tracking was a parallel task making it effective for GPU-based fiber tracking. The conductivity varied due to the direction of the vector. A vector pointing perpendicular to the direction of conductivity indicated slower conductivity compared with a vector pointing the same direction as the conductivity. The fiber orientation was produced by simulating a clinical local activation map as well as the atlas-based mesh of atrial geometry. The fiber orientation was produced by simulating a clinical local activation map as well as the atlas-based mesh of atrial geometry [18,19]. We estimated personalized fiber orientations using an atlas-based method [20,21] to reflect anisotropic conduction from isotropic triangular mesh with 300 μm edges. Then, we adjusted the fiber orientation based on the clinical LAT map. The conductivity of our model [22] was applied 0.1264 S/m (non-

fibrotic longitudinal cell), 0.0546 S/m (fibrotic longitudinal cell), 0.0252 S/m (non-fibrotic transverse cell), and 0.0068 S/m (fibrotic transverse cell). Fibrosis areas were estimated based on the clinical bipolar map. Fibrosis was determined using a nonlinear relationship of the bipolar voltage and the probability of fibrosis. The equation for the probability of fibrosis was described as follows [23]:

$$P_{\text{fibrosis}} = \begin{cases} 1, & \text{X} < 0 \\ -40.0X^3 + 155X^2 - 206X + 99.8 & 0 \le \text{X} \le 1.74 \\ 0, & 1.74 < \text{X} \end{cases}$$

where X is the bipolar voltage at each node, and it was ranged from 0 to 1.74 mV. If X is greater than 1.74 mV, then P_{fibrosis} would be zero. The probability of fibrosis was determined using clinical bipolar voltage data.

Fiber tracking was performed to determine the direction of the conduction. Fibrosis was represented using the relationship between the probability of fibrosis and bipolar voltage values [22]. The diffusion coefficient was calibrated by synchronization of the clinical and virtual conduction velocity. Before a preliminary simulation, conduction velocity was calculated by using the distance from the pacing location to the LA appendage and divided it by the travel time to get the conduction velocity. We then matched conduction velocity from the simulation to clinical conduction velocity by modulating the diffusion coefficient. [18]. A color scale indicating the conduction time was compared between the clinical and virtual activation time maps for matching to produce an accurate conduction environment for each patient.

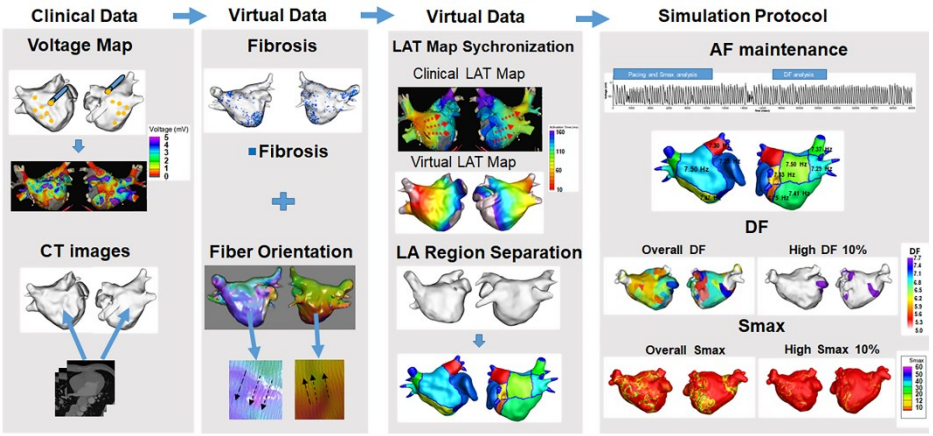

Figure 1. Computational modeling of the left atrium with AF

Realistic LA modeling was conducted using an interpolation of the voltage map and merging with the CT images. Fibrosis and the fiber orientation were implemented. The LAT map synchronization and AF simulation protocol were conducted for the analyses.

3 Virtual AAD intervention

The human atrial myocyte model [24] was used for normal sinus rhythm, and an AF state was created by modifying that model [25]. For the baseline AF state, the I_{Na}, I_{to}, I_{CaL}, I_{Kur}, and I_{Caup} were decreased by 10%, 70%, 70%, 50%, and 20%, and the I_{K1} was increased by 110% as compared to that of the Courtemanche model [25]. Five types of AADs were used for the study. Class III included amiodarone, sotalol, and dronedarone, and class IC indicated flecainide, and propafenone. High dose included amiodarone 10 μM, sotalol 10 mM, dronedarone 10 μM, flecainide 15 μM, and propafenone 10 μM. Low dose included amiodarone 5 μM, sotalol 60 μM, dronedarone 3 μM, flecainide 5 μM, and propafenone 5 μM. All the ionic changes for each drug were derived from previously reported references. Our AAD references used IC50 values. We used such references and make percent changes relative to the Courtemanche-Ramirez-Nattel model [24]. The reduction of channel conductance was calculated to reflect the ion channel blocking effect at the considered concentration. For the implementation of ion currents for each dose, we conducted the literature search and implemented such information to construct the ion currents for each dose as previously reported in our study [10]. As the Courtemanche-Ramirez-Nattel model [26,27] being the baseline, the effects of each dose were implemented by applying the blockage of specific ion channels. Table 1-2 showed detailed descriptions of the ion current changes from baseline in response to the different AADs references including the class IC and class III drugs as well as each dose.

Table 1. AAD Ion currents for Courtemanche Ramirez Nattel model

	‡CRN sinus rhythm										
		Amiodarone		Sotalol		Dronedarone		Flecainide		Propafenone	
	Baseline	5 uM (%)	10 uM (%)	60 uM (%)	10 mM (%)	3 uM (%)	10 uM (%)	5 uM (%)	15 uM (%)	5 uM (%)	10 uM (%)
gNa	100	111	105	95	111	111	100	93	56	86	62
gK1	100	81	72	95	95	90	72	95	95	95	95
gto	100	117	117	117	117	117	117	117	191	261	179
gKr	100	102	90	84	46	102	82	120	120	108	72
gCaL	100	250	225	150	150	200	120	150	215	235	190
gKur	100	200	200	100	100	100	100	120	100	162	96
gKs	100	144	128	144	128	128	96	160	160	160	160
INaCa (Max)	100	155	155	155	155	155	155	155	155	155	155
INaK (Max)	100	100	100	100	100	100	100	100	100	100	100
Iup (Max)	100	100	100	100	100	100	100	100	100	100	100
Krel	100	100	100	100	100	100	100	100	100	100	100
Caup (Max)	100	125	125	125	125	125	125	125	125	125	125
Ach	100	22	15	100	100	100	100	100	100	100	100
	‡CRN AF										
gNa	90	90	85	77	90	90	81	75	45	70	50
gK1	210	180	160	210	210	200	160	210	210	210	210

gto	30	30	30	30	30	30	30	30	49	67	46
gKr	100	85	75	70	38	85	68	100	100	90	60
gCaL	30	50	45	30	30	40	24	30	43	47	38
gKur	50	100	100	50	50	50	50	60	50	81	48
gKs	100	90	80	90	80	80	60	100	100	100	100
INaCa (Max)	100	100	100	100	100	100	100	100	100	100	100
INaK (Max)	100	100	100	100	100	100	100	100	100	100	100
Iup (Max)	100	100	100	100	100	100	100	100	100	100	100
Krel	100	100	100	100	100	100	100	100	100	100	100
Caup (Max)	80	80	80	80	80	80	80	80	80	80	80
Ach	100	22	15	100	100	100	100	100	100	100	100

‡CRN: Courtemanche Ramirez Nattel

Table 2. References for atrial cell ion currents depending on AADs

AADs	Reference	Animal/human model	Method	Ion current change
Flecainide (5 μM, 15 μM)	Geng L. et al., 2018 [28]	Human pluripotent stem cell-derived ventricular cardiomyocyte	Whole-cell patch voltage clamp, microscope, and confocal laser-scanning unit	gNa,gKur,gNa,gto,gCaL
	Yue L. et al., 2000 [29]	Human right atrial appendage		
	Wang Z. et al., 1993 [30]	Human pluripotent stem cell-derived ventricular cardiomyocyte		
	Hilliard FA. et al., 2010 [31]	Canine, murine ventricular model		
Propafenone (5 μM, 10 μM)	Edrich T. et al., 2006 [32]	Human Embryonic kidney cells	Whole-cell patch voltage clamp	gNa, gto, gCaL,gKur, gKr,
	Paul AA. et al., 2002 [33]	Human atrial myocytes		
	A Seki. et al., 1999 [34]	Guinea pig ventricular myocytes		
	Delgado C. et al., 1993 [35]			
Amiodarone (5 μM, 10 μM)	Varela M. et al., 2016 [9]	Canine atrial model	Microelectrode recording and patch-clamp	gK1, gKur, gNa, gKr, gCaL, gKs Ach

Sotalol (60 μM, 10 mM)	Ducroq J. et al., 2007 [36] Lin C. et al., 2007 [37]	Rabbit/Human embronic kidney cells Xenopus oocytes	Bipolar Ag electrode recoding and patch clamp Two-electrode voltage clamp	gNa, gKr, gKs
Dronedarone (3 μM, 10 μM)	Chen KH. et al., 2016 [38] Gautier P. et al., 2003 [39] Ji Y. et al., 2013 [40] Wegender. et al., 2006 [41]	Rat Guinea pig ventricular cardiomyocyte Dog ventricular myocytes Guinea pig myocytes	Whole-cell, perforated patch voltage-clamp	gCaL, gKs, gNa, gK1, gKr, gCaL

4 AF Induction, dominant frequency, and Smax analyses

Our graphic processing unit (GPU)-based customized software (CUVIA ver. 2.5, Model: SH01; Laonmed Inc., Seoul, Korea) was used virtually to induce and apply appropriate ion currents for AADs. The DF and Smax were analyzed using this same GPU-based software. AF was initiated in a pacing location using AF pacing from 200 ms to 120 ms with 8 beats per cycle using ion currents for specific AADs. Virtual pacing location was matched with clinical activation time map for a realistic LA modeling. Before AF induction simulation, clinical and virtual pacing sites were matched to reflect the personalized LA model. Successful AF induction was determined during AF pacing by observing electrogram in the 3D LA map (Figure 2).

Defragmentation of AF includes termination of AF and conversion of AF to atrial tachycardia. Defragmentation was determined by visually assessing the electrogram and 3D activation map of each case. If there were less than two spiral waves, we determined it as a defragmented state. Once AF was induced successfully, maintenance of AF was observed up to 32 secs. During the maintenance period, the DF was calculated from 17 sec to 23 sec. APD_{90} was a normal sinus rhythm measured at a pacing cycle length of 600 ms. We calculated using non-linear fitting of APD_{90} and diastolic interval [42] from over 400,000 nodes during single-site pacing. Smax values were defined at every node in LA regions per patient. For the regional analyses of the Smax and DF, the LA was divided into 10 regions. 10 regions of LA were decided based on the previous clinical study [43]. We used 3D spiral CT images of LA to divide LA portions according to the embryological origin. The portions include the

venous LA (posterior LA including the antrum and posterior wall), anterior LA (excluding LA appendage), and LAA. We also divided PV antrum, posterior inferior wall, and septum along the posterior inferior line and septal line. The mean DF and mean Smax were calculated using the results of all 10 regions. A high DF and high Smax were defined as the respective top 10% of the values (Figure 3-4). For the stability of the DF and Smax after AADs, the coefficient of variation (COV) of the high DF and high Smax were calculated as the standard deviation divided by the mean:

$$\text{COV} = \frac{\sigma}{\overline{x}}$$

σ represented the standard deviation, and $\overline{x}$ indicated the mean value.

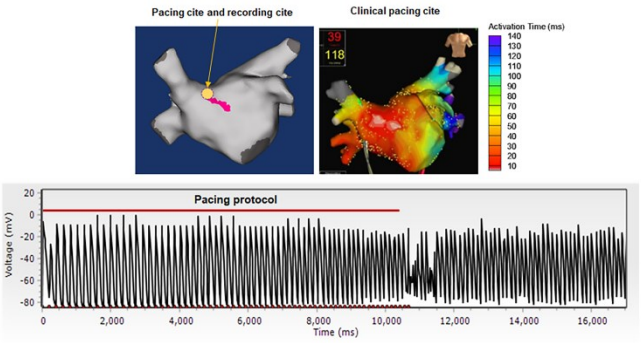

Figure 2. Pacing and recording location of electrogram

The representative electrograms were taken from the pacing site, which corresponded with the earliest activation site on the clinical local activation time (LAT) map during right atrial pacing (Bachmann's bundle activation site).

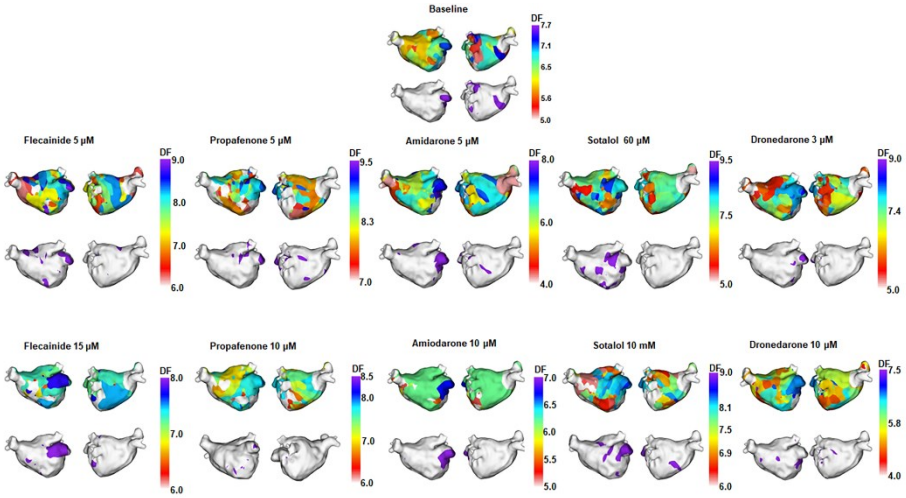

Figure 3. Overall 3D DF maps and high DF areas

3D DF maps indicated overall DF, and high DF areas from baseline to AADs.

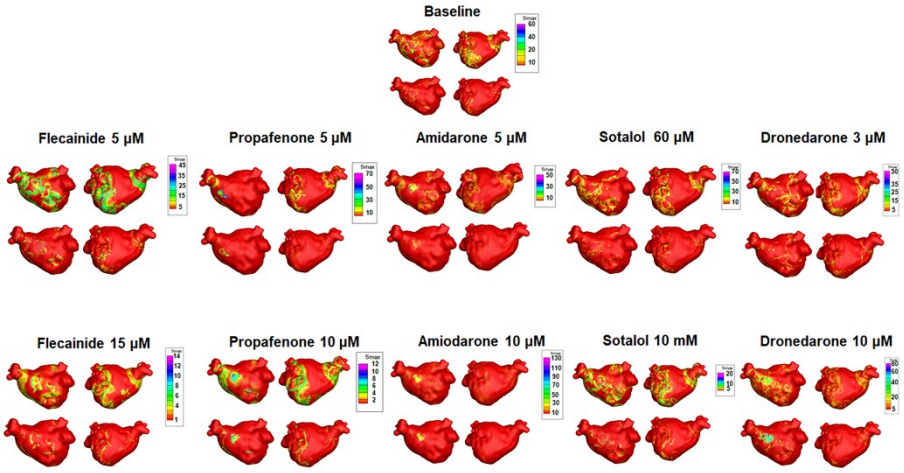

Figure 4. Overall 3D Smax, and high Smax areas

3D Smax maps demonstrated overall Smax, and high Smax areas from baseline to AADs

5 Statistical analyses

The continuous variables were represented as the median and interquartile range. A comparison of the DF, Smax, and COV was conducted using a t-test and Mann-Whitney test depending on the distribution. A p-value less than 0.05 was considered statistically significant. Any case in which the DF terminated before 17 seconds was excluded from the study. Statistical analyses were conducted using SPSS (IBM Corp., IBM SPSS Statistics for Windows, Version 21.0) and Rstudio (RStudio Team [2020]. RStudio: Integrated Development for R. RStudio, PBC, Boston, MA URL http://www.rstudio.com/) software.

III. RESULTS

1 Effects of AADs on the AF wave-dynamics

The patient group consisted of 25 AF patients (68.0% male, 59.8±9.8 years old, 32.0% paroxysmal AF) who had undergone radiofrequency catheter ablation (Table 3). Table 4 compared the effects of AADs on the electrophysiological parameters and wave-dynamic parameters. Overall (2 class IC and 3 class III AADs, low and high doses for each drug), the AADs prolonged the action potential duration for the 90% repolarization (APD_{90}, $p<0.001$) and mean AF cycle length (AFCL, $p<0.001$) and reduced the conduction velocity (CV, $p=0.007$), but did not change the Smax ($p=0.899$). The DF ($p<0.001$) and COV-DF ($p=0.001$, Figure 5) reduction effects of the class III AAD were more significant than those of the class IC AADs (Table 4). AADs dose-dependently changed the APD_{90} ($p<0.001$), AFCL ($p<0.001$), and CV ($p<0.001$), and the DF reduction was more pronounced at high doses than low doses ($p<0.001$, Table 4).

Table 3. Baseline characteristics

Characteristics	N=25
Male, n (%)	17 (68.0%)
Age, (Years)	59.8±9.8
<65, n (%)	14 (56.0%)
65–74, n (%)	10 (40.0%)
≥75, n (%)	1 (4.0%)
Paroxysmal AF, n (%)	8 (32.0%)
Follow-up Duration, (Months)	14.2±15.3
BMI, (Kg/m^2)	24.6±2.9
CHA_2DS_2-VASc Score	2.0±1.4
Heart failure, n (%)	3 (12.0%)
Hypertension, n (%)	11 (44.0%)
Diabetes, n (%)	4 (16.0%)
Stroke/TIA, n (%)	5 (20.0%)
Vascular Disease, n (%)	2 (8.0%)
Echocardiographic Parameters	
LA Dimension, (mm)	42.6±6.1
LA Volume Index, (mL/m^2)	40.4±9.2
LVEF (%)	63.6±6.8
E/Em	10.6±3.8
LA Voltage, (mV)	1.9±0.8

BMI: Body Mass Index, TIA: Transient Ischemic Attack, LVEF: Left Ventricular Ejection Fraction, E: Early Diastolic Transmitral Flow Velocity, Em: Early Diastolic Mitral Annular Velocity.

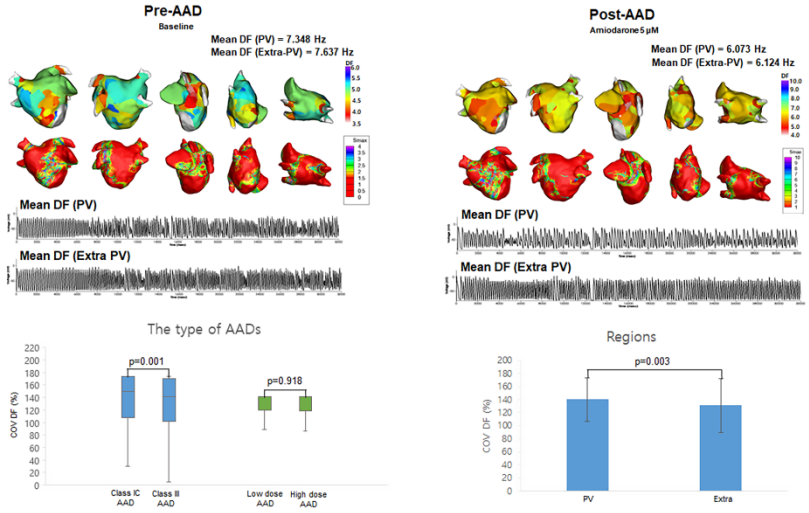

Figure 5. The effects of AADs on extra-PV and PV regions
The 3D DF map indicated that the mean DF was higher in the PV regions. Electrograms demonstrated regional voltage changes in PV and extra-PV areas. COV-DF was higher in class IC and PV region.

Table 4. Effects of AADs on the electrophysiological and fibrillatory wave-dynamics parameters

	Baseline (†n=25)	Overall AADs (†n=250)	p-value	Class IC AADs (†n=100)	Class III AADs (†n=150)	p-value	Low dose AADs (†n=125)	High dose AADs (†n=125)	p-value
APD_{90}, (ms)	233.000 [231.000,239.000]	273.000 [263.000,295.000]	<0.001	269.000 [256.000,290.000]	277.000 [265.000,303.000]	0.002	267.000 [261.000,273.000]	293.000 [271.000,309.000]	<0.001
CV, (m/s)	0.750 [0.617,0.906]	0.612 [0.411,0.741]	0.007	0.598 [0.474,0.732]	0.618 [0.395,0.745]	0.615	0.674 [0.484,0.826]	0.526 [0.346,0.685]	<0.001
Mean AFCL, (ms)	135.616 [130.526,150.303]	159.344 [145.632,176.964]	<0.001	156.508 [140.000,171.579]	162.312 [150.923,183.952]	0.038	153.750 [140.000,172.281]	164.167 [156.508,192.404]	<0.001
Mean Smax	0.785 [0.656,0.963]	0.802 [0.635,1.009]	0.899	0.851 [0.639,1.027]	0.744 [0.629,0.998]	0.136	0.730 [0.628,0.916]	0.851 [0.677,1.106]	0.003
Mean DF, (Hz)	7.025 [6.097,7.379]	5.722 [1.286,6.553]	<0.001	6.148 [5.315,6.922]	5.170 [1.200,6.145]	<0.001	6.121 [5.082,6.874]	5.101 [1.200,6.098]	<0.001

COV-DF, (%)	NA	141.421 [105.265,173.205]	NA	149.079 [108.095,173.205]	141.421 [102.270,170.349]	0.001	141.000 [120.000,141.000]	141.000 [119.000,141.000]	0.918

APD_{90}: Action potential duration 90%, CV: Conduction velocity, AFCL: AF cycle length, Smax: The Maximal slope of the restitution curves, DF: Dominant frequency, COV-DF: Coefficient of Variation-Dominant Frequency
Note: Patients who did not sustain proper normal sinus rhythm and an AF status were excluded from the analysis.
Median [IQ1,IQ3]
†n= The number of patients *AAD*Dose

2 Different AAD effects on the PV and extra-PV regions

Among the 10 segments of the LA, we compared the areas of the PV antrum and extra-PV regions (Table 5). The Smax and DF did not differ between the PV antrum and extra-PV LA regions during the baseline AF. After the administration of the AADs, the mean DF became lower ($p<0.001$, Figure 5) and COV-DF higher ($p=0.003$, Figure 5) at the PV antrum than in extra-PV LA regions, which suggested a lower and unstable DF on the PV antrum after AADs.

Table 5. Effects of AADs on the PV vs. Extra-PV tissue

	Baseline			AAD		
	PV (†n=25)	**Extra-PV (†n=25)**	**p-value**	**PV (†n=750)**	**Extra-PV (†n=500)**	**p-value**
Mean Smax	1.258 [1.060,1.619]	1.418 [1.006,1.729]	0.541	1.264 [0.802,1.659]	1.290 [0.892,1.663]	0.541
ΔMean Smax	NA	NA	NA	-0.027 [-0.219,0.170]	0.006 [-0.326,0.250]	0.692
Mean DF, (Hz)	7.567 [6.246,8.186]	7.916 [7.383,8.595]	0.086	6.464 [5.246,7.170]	7.029 [6.209,7.659]	<0.001
ΔMean DF	NA	NA	NA	-0.820 [-1.275,-0.236]	-0.848 [-1.368,-0.298]	0.238
COV-DF, (%)	NA	NA	NA	141.421 [117.963,173.205] ‡140.446 ± 33.227	141.421 [97.825,172.515] ‡130.932 ± 41.633	0.003

Smax: The Maximal slope of the restitution curves, ΔMean Smax: Changes of Smax, DF: Dominant Frequency, ΔMean DF: Changes of DF, COV-DF: Coefficient of Variation-Dominant Frequency
Note: Patients who did not sustain proper normal sinus rhythm and an AF status were excluded from the analysis.
Median [IQ1,IQ3]
†n= The number of patients *AAD*Dose
‡Mean±SD

3 Post-AAD mean DF depending on the Smax

We compared the changes in the mean DF and COV-DF at a Smax value of 1.4, based on a previous clinical study for human atrial restitution (Table 6). In Table 6, we used the baseline Smax values threshold for baseline mean DF, and post-AAD Smax threshold for post-AAD mean DF. At a Smax ≥1.4, the post-AAD mean DF was significantly lower than that at a Smax <1.4 ($p=0.014$, Figure 6). The pattern of a higher mean DF during a Smax <1.4 condition was consistent in the PV ($p=0.039$, Figure 6) and extra-PV areas ($p=0.002$, Figure 6). However, the COV-DFs did not differ depending on the Smax value. Additionally, we differentiated especially Table 6 into subgroups as indicated in Table 7. DF was higher in dronedarone 3 μM and amiodarone 5 μM at low Smax.

Table 6. AF wave-dynamics depending on the Smax values

	Overall		p-value	PV		p-value	Extra-PV		p-value
	Smax < 1.4 (†n=13)	**Smax ≥ 1.4 (†n=12)**		**Smax < 1.4 (†n=13)**	**Smax ≥ 1.4 (†n=12)**		**Smax < 1.4 (†n=13)**	**Smax ≥ 1.4 (†n=12)**	
Baseline Mean DF, (Hz)	7.958 [7.138,8.485]	7.708 [7.194,8.013]	0.650	7.797 [6.246,8.243]	7.338 [6.382,8.061]	0.689	8.103 [7.796,8.599]	7.836 [7.220,8.385]	0.503
Post-AAD Mean DF (Hz)	6.986 [6.011,7.677]	6.584 [5.801,7.015]	0.014	6.732 [5.013,7.534]	5.963 [5.430,6.815]	0.039	7.225 [6.411,7.781]	6.818 [5.859,7.168]	0.002
Post-AAD COV-DF, (%)	141.000 [104.000,141.000]	141.000 [110.000,141.000]	0.656	141.000 [116.500,141.000]	141.000 [131.500,141.000]	0.532	141.000 [96.600,141.000]	140.000 [91.900,141.000]	0.371

DF: Dominant Frequency, COV-DF: Coefficient of Variation.
Note: Patients who did not sustain proper normal sinus rhythm and an AF status were excluded from the analysis.
Median [IQ1, IQ3]
†n= The number of patients *AAD*Dose

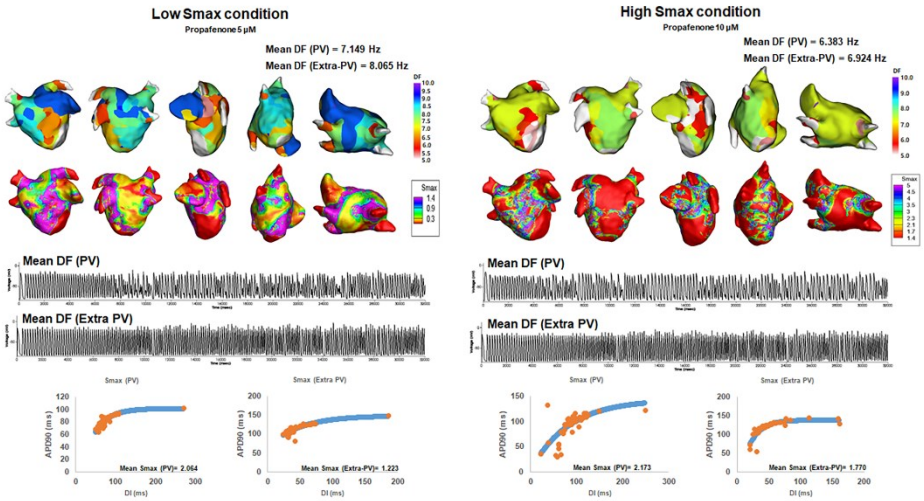

Figure 6. Changes in the DF during a high and low Smax

The 3D DF map indicated that the mean DF was inversely related to the mean Smax. Regional voltage changes in PV and extra-PV areas were demonstrated in electrograms.

Table 7. AF wave-dynamics depending on the Smax values with AADs

	Overall		p-value	PV		p-value	Extra-PV		p-value
	Smax < 1.4 (†n=13)	Smax ≥ 1.4 (†n=12)		Smax < 1.4 (†n=13)	Smax ≥ 1.4 (†n=12)		Smax < 1.4 (†n=13)	Smax ≥ 1.4 (†n=12)	
Baseline Mean DF, (Hz)	7.958 [7.138,8.485]	7.708 [7.194,8.013]	0.650	7.797 [6.246,8.243]	7.338 [6.382,8.061]	0.689	8.103 [7.796,8.599]	7.836 [7.220,8.385]	0.503
Post-AAD Mean DF (Hz)	6.986 [6.011,7.677]	6.584 [5.801,7.015]	0.014	6.732 [5.013,7.534]	5.963 [5.430,6.815]	0.039	7.225 [6.411,7.781]	6.818 [5.859,7.168]	0.002
Flecainide 5 μM	8.203 [6.558-8.389]	7.167 [6.348-7.419]		8.115 [5.318-8.312]	6.258 [6.013-6.955]		8.419 [7.621-8.664]	7.443 [6.366-7.594]	
Flecainide 15 μM	6.452 [5.436-6.920]	6.707 [6.443-7.015]		5.722 [4.697-6.711]	6.815 [5.862-6.831]		6.780 [5.970-7.237]	6.816 [6.663-7.168]	
Propafenone 5 μM	7.730 [6.891-8.174]	6.573 [6.127-7.019]		7.585 [5.939-8.098]	5.794 [5.723-5.866]		7.842 [7.551-8.293]	6.806 [6.249-7.363]	
Propafenone 10 μM	7.106 [6.332-7.166]	6.828 [6.560-6.971]		6.993 [4.899-7.093]	6.820 [5.519-6.988]		7.216 [7.175-7.327]	6.943 [6.924-6.963]	
Amiodarone 5 μM	7.005 [6.251-7.213]	6.060 [5.689-6.085]	0.022	6.803 [6.040-7.032]	5.281 [5.042-5.677]		7.170 [6.390-7.385]	6.124 [5.798-6.255]	<0.001
Amiodarone 10 μM	5.432 [3.316-5.584]	5.705 [5.548-5.821]		5.425 [3.312-5.469]	5.292 [4.847-5.730]		5.435 [3.317-5.625]	5.877 [5.611-6.073]	
Sotalol 60 μM	7.551 [7.190-7.961]	7.071 [6.294-7.200]		7.345 [6.930-7.835]	6.590 [5.732-6.971]		7.774 [7.666-8.019]	7.242 [6.287-7.455]	

Sotalol 10 mM	7.193 [5.262-7.673]	6.880 [6.626-6.920]		7.269 [4.119-7.433]	6.082 [5.697-6.551]		7.151 [5.239-7.787]	7.011 [6.799-7.135]	
Dronedarone 3 μM	7.080 [6.824-7.462]	5.890 [1.298-6.490]	0.001	6.969 [6.530-7.220]	5.606 [1.296-6.080]	0.013	7.485 [6.964-7.586]	6.122 [1.299-6.643]	<0.001
Dronedarone 10 μM	5.707 [3.863-6.288]	5.967 [5.627-6.592]		3.712 [2.220-5.794]	5.361 [4.766-6.339]		6.129 [4.399-6.378]	6.146 [5.862-6.806]	
Post-AAD COV-DF, (%)	141.000 [104.000,141.000]	141.000 [110.000,141.000]	0.656	141.000 [116.500,141.000]	141.000 [131.500,141.000]	0.532	141.000 [96.600,141.000]	140.000 [91.900,141.000]	0.371

DF: Dominant Frequency, COV-DF: Coefficient of Variation.
Note: Patients who did not sustain proper normal sinus rhythm and an AF status were excluded from the analysis.
Median [IQ1, IQ3]
†n= The number of patients *AAD*Dose

4 Termination or defragmentation of AF depending on the DF and COV-DF

Table 8 shows the electrophysiological characteristics of the termination and defragmentation episodes of AF after the AAD administration. In the episodes of AF defragmentation within 32 sec after the AAD administration, the mean DF was significantly lower ($p<0.001$, Table 8, Figure 4), and the COV-DF was significantly higher ($p<0.001$, Figure 7) than that in those with sustained AF. In the AF termination episodes, the mean DF was consistently lower ($p<0.001$, Table 8) and COV-DF higher ($p<0.001$, Figure 7). The tendency of a low DF and unstable (higher) COV-DF in the AF defragmentation episodes was consistent regardless of the class IC or class III AAD (Table 8).

Table 8. Electrophysiological characteristics terminated AF after AADs

Defragmentation	Oveall AADs			Class IC			Class III		
	Defragmented (†n=290)	Not defragmented (†n=2210)	p-value	Defragmented (†n=60)	Not defragmented (†n=940)	p-value	Defragmented (†n=230)	Not defragmented (†n=1270)	p-value
Mean Smax	1.254 [1.022,1.526]	1.263 [0.923,1.675]	0.777	1.275 [0.920,1.509]	1.271 [0.901,1.549]	0.894	1.238 [1.036,1.507]	1.255 [0.941,1.856]	0.729
Mean DF, (Hz)	5.476 [1.299,6.706]	6.913 [6.233,7.466]	<0.001	5.770 [5.201,6.563]	7.118 [6.527,7.860]	0.029	5.262 [1.299,6.640]	6.710 [5.992,7.227]	<0.001
COV-DF, (%)	141.000 [139.000,141.000] ‡126.166± 33.607	141.000 [108.500,141.000] ‡117.571±39.203	<0.001	141.000 [140.750,141.000] ‡136.285 ± 10.847	141.000 [109.750,141.000] ‡117.432 ± 39.783	<0.001	141.000 [138.250,141.000] ‡123.734 ± 36.821	141.000 [98.625,141.000] ‡115.311±40.276	0.008
Termination	**Oveall AADs**			**Class IC**			**Class III**		
	Terminated (†n=230)	Not Terminated (†n=2270)	p-value	Terminated (†n=30)	Not Terminated (†n=970)	p-value	Terminated (†n=200)	Not Terminated (†n=1300)	p-value
Mean Smax	1.265 [1.041,1.437]	1.263 [0.901,1.675]	0.704	0.812 [0.809,1.059]	1.264 [0.900,1.552]	0.281	1.294 [1.089,1.481]	1.255 [0.941,1.856]	0.885

Mean DF, (Hz)	5.295 [1.299,6.677]	6.889 [6.170,7.465]	<0.001	5.041 [3.170,6.896]	7.101 [6.469,7.843]	0.385	5.476 [1.299,6.677]	6.170 [5.507,6.684]	0.084
COV-DF, (%)	141.000 [139.500,141.000] ‡126.312±33.185	141.000 [103.000,141.000] ‡116.545±40.083	<0.001	141.000 [136.000,141.000] ‡131.124±19.179	141.000 [113.000,141.000] ‡118.718±38.890	0.199	141.000 [141.000,141.000]	138.000 [85.750,141.000]	<0.001

Smax: The Maximal slope of the restitution curves, DF: Dominant Frequency, COV-DF: Coefficient of Variation-Dominant Frequency
Defragmentation: Termination + Atrial Tachycardia
Note: Patients who did not sustain proper normal sinus rhythm and an AF status were excluded from the analysis.
Median [IQ1, IQ3]
†n= The number of patients *AAD*Dose
‡Mean±SD

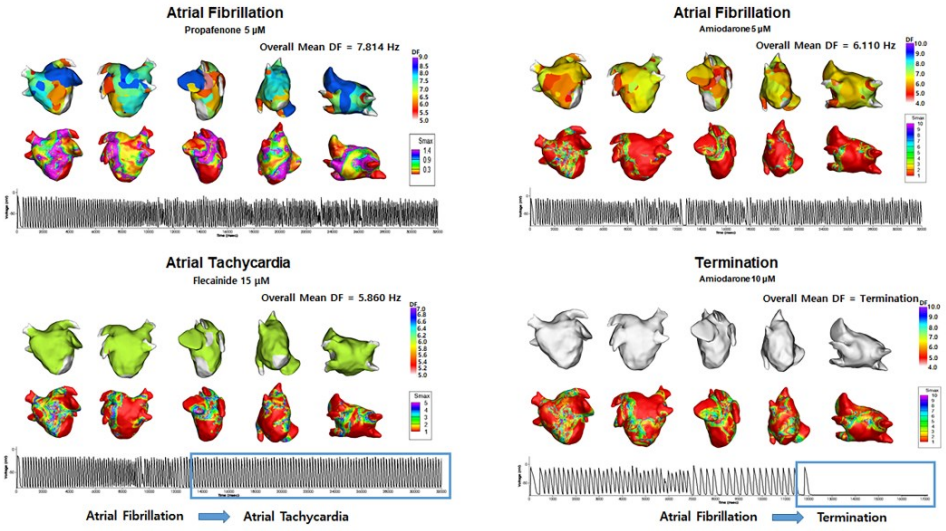

Figure 7. Changes in the DF during Termination and Atrial Tachycardia

The 3D DF map indicated that the mean DF was lower during AT episodes, and AF termination episodes. Electrograms demonstrated AT and AF termination episodes.

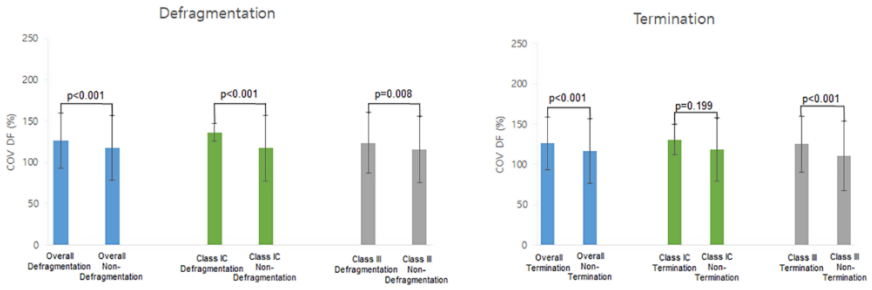

Figure 8. Heterogeneity of DF

Heterogeneity of DF was observed in overall defragmentation as well as termination group.

IV. DISCUSSION

1 Main findings

We evaluated the spatial changes in the AF wave-dynamics reflected by the mean DF and COV-DF after using AADs in a realistic computational model that reflected 25 AF patients' LA geometry, histology, and electrophysiology. The AAD classes and doses apparently affected the AF wave-dynamics, and those effects differed between the PV and extra-PV regions depending on the Smax. The AADs easily caused defragmentation or termination at a reduced mean DF and spatially unstable DF (high COV-DF). Realistic AF computational modeling was a feasible approach to study the regional effect of AADs or electrophysiological changes.

2 Anti-AF effects of AADs on the PV or extra-PV regions

The mechanism of the AADs involves the blocking of specific trans-membrane ion channels to inhibit the initiation or maintenance mechanisms of fibrillation. Class IC drugs function by blocking the rapid inward sodium current that slows the rate of the increasing action potential, and class III AADs block the outward potassium current, lengthening the repolarization and refractoriness [44]. However, it is not known how AADs act on different regions of the atrium and how the wave-dynamics react according to the anatomical structure. There have been many studies on the role of the PVs in the mechanism of AF [45]. The PVs have a venous atrium origin that differs from that of other parts of the atrium in terms of the embryological development [46] and are influenced highly by AF-associated genes such as *PITX2* [47]. For this reason,

the electrical isolation of the PV antrum is the most important target for AF catheter ablation [48]. PV isolation blocks not only the triggers from the PVs, but also the cardiac autonomic nerves located in the PV antrum and reduces the atrial critical mass. In this study, AADs reduced the mean DF and its spatial instability (COV-DF) more significantly in the PV area than non-PV area. That suggested that the anti-AF effect of AADs mainly is responsible for the lower and spatially unstable DFs in the PV area than in the extra-PV areas. Investigation of the select effects of AADs on the LA regions can have a significant impact on the treatment of AF.

3 AF mechanisms of multiple wavelet or focal sources

The focal source hypothesis and multiple wavelet hypothesis have been considered as mechanisms of AF initiation and maintenance [49,50]. The focal source hypothesis indicates that a special form of a reentry pattern of activation produced by rotors drives the AF mechanism. The multiple wavelet hypothesis explains the AF mechanism as spontaneous wave-breaks that constantly generate randomly wandering daughter wavelets. These wave-breaks collide, are disrupted, coalesce, or give rise to new wavelets in a self-sustaining turbulent process [51]. High DF areas were used to locate the source of AF drivers or rotors [52], and high Smax areas represent the vulnerable condition of AF wave-breaks in the AF maintenance mechanism [53]. Therefore, the DF is a representative parameter for the focal source hypothesis, and the Smax advocates the multiple wavelet theory. Wu et al. reported that the focal source and multiple wavelets interact and maintain fibrillation according to the tissue

conditions such as the conduction velocity [54]. The present study demonstrated for the first time that the Smax has a direct effect on the DF wave-dynamics in AF and anti-AF mechanisms. Although the AADs did not decrease the Smax, the focal source mechanism represented by the DF was predominant in maintaining AF in atrial tissue with a low Smax. At a low Smax, the mean DF was high in both the PV and extra-PV regions, whereas the mean DF was low when the Smax was high. Therefore, the DF and Smax exhibited an inverse relationship.

4 Sufficient conditions for AF defragmentation or termination

Many studies [14,55,56] have been conducted over the years to understand spiral wave meander and AF termination in various ways. After the AADs, the continuous wave-breaks and reentrant behaviors could not be sustained, resulting in termination or defragmentation. Though a spiral meandering and reentry termination are challenging to study quantitatively [55], we analyzed the DF and Smax changes during the AF defragmentation using realistic computational modeling of AF. This is because the computational modeling enabled spatiotemporally high-resolution mapping while repeatedly being performed [10,12]. In this study, the changes in the DF wave-dynamics had a close relationship with the AF defragmentation. The defragmented AF episodes after the virtual AAD intervention exhibited a reduced mean DF and high COV-DF (spatial instability of DF) regardless of the type of AAD. These changes in the DF were consistently observed in the AF termination episodes. The change in the Smax did not have a direct effect on the AF termination, which was presumably because the

AADs did not significantly change the Smax.

5 Limitations

RA was omitted from the study. The biatrial model is premature to be applied in personalized modeling because current image resolution cannot define the personalized interatrial connections. Heterogeneity due to nervous influence has been neglected. The fiber orientation layer was a monolayer. The LA wall thickness can be implemented to reflect a more clinically acceptable LA model. Bipolar voltage was not a feasible marker for fibrosis, and fiber orientation was not measured in a patient-specific manner. To incorporate a clinical electroanatomical map to the high-resolution computational modeling, we heavily extrapolated the limited number of bipolar electrograms. We measured DF at a fixed time window and it did not change over time. Regions especially PV specific ionic currents were not applied in this study due to lack of reference for ion currents effects of AADs on PV cells. No focal triggers were simulated in this study. The personalized LA model consisted of a monolayer. The LA wall thickness can be implemented to reflect a more clinically acceptable LA model. Multiple induction sites can reflect the complex mechanism of AF initiation [57]. Although there are some differences in the rate-dependent action potential changes, restitution, and calcium dynamics among different human myocardial cell models, [27,58-60] the Courtemanche-Ramirez-Nattel model [26, 27] accurately represented the mathematical modeling of human atrial myocyte as indicated in our previous studies [10,11,18,23,25,52]. The ion currents conductance values might not be an accurate

representation of the effects of AADs in human atrial myocytes, however, the amount of uncertainty was minimal since large mammals were selected for references (Table 2). Invasive mapping data were used for the analysis. Non-invasive late gadolinium enhancement of the cardiac magnetic resonance imaging data can be used for further analysis [61]. Artificial intelligence can also be used to replace invasive mapping data. Clinical validation of computation modeling of AAD effects is required for further studies. Ion currents derived from human models will be ideal for future computational modeling.

V. CONCLUSION

A DF reduction due to AADs is predominantly observed in the PV regions, and the AAD-induced low and heterogeneous DF condition during a high Smax condition was associated with AF termination or defragmentation. Realistic AF computational modeling provided convincing evidence of how AADs exhibit anti-AF effects according to the atrial region or electrophysiological condition.

REFERENCES

1. Kim D, Yang PS, Jang E, Yu HT, Kim TH, Uhm JS, et al. 10-year nationwide trends of the incidence, prevalence, and adverse outcomes of non-valvular atrial fibrillation nationwide health insurance data covering the entire Korean population. Am Heart J 2018;202:20-6.
2. Cardiac-Arrhythmia-Suppression-Trial-(CAST)-Investigators. Preliminary report: effect of encainide and flecainide on mortality in a randomized trial of arrhythmia suppression after myocardial infarction. N Engl J Med 1989;321:406-12.
3. The-AFFIRM-Investigators. Relationships Between Sinus Rhythm, Treatment, and Survival in the Atrial Fibrillation Follow-Up Investigation of Rhythm Management (AFFIRM) Study. Circulation 2004;109:1509-13.
4. Chandhok S, Schwartzman D. Amiodarone therapy for atrial rhythm control: insights gained from a single center experience. J Cardiovasc Electrophysiol 2007;18:714-8.
5. Hindricks G, Potpara T, Dagres N, Arbelo E, Bax JJ, Blomström-Lundqvist C, et al. 2020 ESC Guidelines for the diagnosis and management of atrial fibrillation developed in collaboration with the European Association for Cardio-Thoracic Surgery (EACTS): The Task Force for the diagnosis and management of atrial fibrillation of the European Society of Cardiology (ESC) Developed with the special contribution of the European Heart Rhythm Association (EHRA) of the ESC. European Heart Journal 2021;42:373-498.
6. Kirchhof P, Camm AJ, Goette A, Brandes A, Eckardt L, Elvan A, et al. Early Rhythm-Control Therapy in Patients with Atrial Fibrillation. New England Journal of Medicine 2020;383:1305-16.
7. Darbar D, Roden DM. Genetic mechanisms of atrial fibrillation: impact on response to treatment. Nat Rev Cardiol 2013;10:317-29.
8. Roy D, Talajic M, Dorian P, Connolly S, Eisenberg MJ, Green M, et al. Amiodarone to Prevent Recurrence of Atrial Fibrillation. New England Journal of Medicine 2000;342:913-20.
9. Varela M, Colman MA, Hancox JC, Aslanidi OV. Atrial Heterogeneity Generates Re-entrant Substrate during Atrial Fibrillation and Anti-arrhythmic Drug Action: Mechanistic Insights from Canine Atrial Models. PLoS Comput Biol 2016;12:e1005245.
10. Hwang I, Park J-W, Kwon O-S, Lim B, Hong M, Kim M, et al. Computational Modeling for Antiarrhythmic Drugs for Atrial Fibrillation According to Genotype. Frontiers in Physiology 2021;12.
11. Lim B, Park JW, Hwang M, Ryu AJ, Kim IS, Yu HT, et al. Electrophysiological significance of the interatrial conduction including cavo-tricuspid isthmus during atrial fibrillation. J Physiol 2020;598:3597-612.
12. Li C, Lim B, Hwang M, Song J-S, Lee Y-S, Joung B, et al. The

Spatiotemporal Stability of Dominant Frequency Sites in In-Silico Modeling of 3-Dimensional Left Atrial Mapping of Atrial Fibrillation. PLOS ONE 2016;11:e0160017.

13. Loewe A, Lutz Y, Wilhelms M, Sinnecker D, Barthel P, Scholz EP, et al. In-silico assessment of the dynamic effects of amiodarone and dronedarone on human atrial patho-electrophysiology. Europace 2014;16 Suppl 4:iv30-iv8.
14. Bai J, Zhu Y, Lo A, Gao M, Lu Y, Zhao J, et al. In Silico Assessment of Class I Antiarrhythmic Drug Effects on Pitx2-Induced Atrial Fibrillation: Insights from Populations of Electrophysiological Models of Human Atrial Cells and Tissues. Int J Mol Sci 2021;22.
15. Jarman JW, Wong T, Kojodjojo P, Spohr H, Davies JE, Roughton M, et al. Spatiotemporal behavior of high dominant frequency during paroxysmal and persistent atrial fibrillation in the human left atrium. Circ Arrhythm Electrophysiol 2012;5:650-8.
16. Kogawa R, Okumura Y, Watanabe I, Kofune M, Nagashima K, Mano H, et al. Spatial and temporal variability of the complex fractionated atrial electrogram activity and dominant frequency in human atrial fibrillation. Journal of arrhythmia 2015;31:101-7.
17. Ugarte JP, Tobón C, Orozco-Duque A, Becerra MA, Bustamante J. Effect of the electrograms density in detecting and ablating the tip of the rotor during chronic atrial fibrillation: an in silico study. Europace 2015;17 Suppl 2:ii97-104.
18. Lim B, Kim J, Hwang M, Song J-S, Lee JK, Yu H-T, et al. In situ procedure for high-efficiency computational modeling of atrial fibrillation reflecting personal anatomy, fiber orientation, fibrosis, and electrophysiology. Sci Rep 2020;10:2417.
19. Pashakhanloo F, Herzka DA, Ashikaga H, Mori S, Gai N, Bluemke DA, et al. Myofiber Architecture of the Human Atria as Revealed by Submillimeter Diffusion Tensor Imaging. Circ Arrhythm Electrophysiol 2016;9:e004133.
20. Niederer SA, Lumens J, Trayanova NA. Computational models in cardiology. Nature reviews. Cardiology 2019;16:100-11.
21. Roney CH, Bendikas R, Pashakhanloo F, Corrado C, Vigmond EJ, McVeigh ER, et al. Constructing a Human Atrial Fibre Atlas. Ann Biomed Eng 2021;49:233-50.
22. Zahid S, Cochet H, Boyle PM, Schwarz EL, Whyte KN, Vigmond EJ, et al. Patient-derived models link re-entrant driver localization in atrial fibrillation to fibrosis spatial pattern. Cardiovasc Res 2016;110:443-54.
23. Hwang M, Kim J, Lim B, Song J-S, Joung B, Shim EB, et al. Multiple factors influence the morphology of the bipolar electrogram: An in silico modeling study. PLoS Comput Biol 2019;15:e1006765.
24. Courtemanche M, Ramirez RJ, Nattel S. Ionic mechanisms underlying human atrial action potential properties: insights from a mathematical model. Am J Physiol 1998;275:H301-21.
25. Lee YS, Hwang M, Song JS, Li C, Joung B, Sobie EA, et al. The Contribution

of Ionic Currents to Rate-Dependent Action Potential Duration and Pattern of Reentry in a Mathematical Model of Human Atrial Fibrillation. PLoS One 2016;11:e0150779.

26. Sossalla S, Kallmeyer B, Wagner S, Mazur M, Maurer U, Toischer K, et al. Altered Na+Currents in Atrial Fibrillation: Effects of Ranolazine on Arrhythmias and Contractility in Human Atrial Myocardium. Journal of the American College of Cardiology 2010;55:2330-42.
27. Grandi E, Pandit SV, Voigt N, Workman AJ, Dobrev D, Jalife J, et al. Human atrial action potential and Ca2+ model: sinus rhythm and chronic atrial fibrillation. Circ Res 2011;109:1055-66.
28. Geng L, Kong CW, Wong AOT, Shum AM, Chow MZY, Che H, et al. Probing flecainide block of I(Na) using human pluripotent stem cell-derived ventricular cardiomyocytes adapted to automated patch-clamping and 2D monolayers. Toxicol Lett 2018;294:61-72.
29. Yue L, Feng JL, Wang Z, Nattel S. Effects of ambasilide, quinidine, flecainide and verapamil on ultra-rapid delayed rectifier potassium currents in canine atrial myocytes. Cardiovasc Res 2000;46:151-61.
30. Wang Z, Fermini B, Nattel S. Mechanism of flecainide's rate-dependent actions on action potential duration in canine atrial tissue. J Pharmacol Exp Ther 1993;267:575-81.
31. Hilliard FA, Steele DS, Laver D, Yang Z, Le Marchand SJ, Chopra N, et al. Flecainide inhibits arrhythmogenic Ca2+ waves by open state block of ryanodine receptor Ca2+ release channels and reduction of Ca2+ spark mass. J Mol Cell Cardiol 2010;48:293-301.
32. Edrich T, Wang SY, Wang GK. State-dependent block of human cardiac hNav1.5 sodium channels by propafenone. J Membr Biol 2005;207:35-43.
33. Paul AA, Witchel HJ, Hancox JC. Inhibition of the current of heterologously expressed HERG potassium channels by flecainide and comparison with quinidine, propafenone and lignocaine. Br J Pharmacol 2002;136:717-29.
34. Seki A, Hagiwara N, Kasanuki H. Effects of propafenone on K currents in human atrial myocytes. Br J Pharmacol 1999;126:1153-62.
35. Delgado C, Tamargo J, Henzel D, Lorente P. Effects of propafenone on calcium current in guinea-pig ventricular myocytes. Br J Pharmacol 1993;108:721-7.
36. Ducroq J, Printemps R, Guilbot S, Gardette J, Salvetat C, Le Grand M. Action potential experiments complete hERG assay and QT-interval measurements in cardiac preclinical studies. J Pharmacol Toxicol Methods 2007;56:159-70.
37. Lin C, Ke X, Cvetanovic I, Ranade V, Somberg J. The Effect of High Extracellular Potassium on IKr Inhibition by Anti-Arrhythmic Agents. Cardiology 2007;108:18-27.
38. Chen KH, Xu XH, Sun HY, Du XL, Liu H, Yang L, et al. Distinctive property and pharmacology of voltage-gated sodium current in rat atrial vs ventricular myocytes. Heart Rhythm 2016;13:762-70.
39. Gautier P, Guillemare E, Marion A, Bertrand JP, Tourneur Y, Nisato D.

Electrophysiologic characterization of dronedarone in guinea pig ventricular cells. J Cardiovasc Pharmacol 2003;41:191-202.
40. Ji Y, Takanari H, Qile M, Nalos L, Houtman MJC, Romunde FL, et al. Class III antiarrhythmic drugs amiodarone and dronedarone impair KIR 2.1 backward trafficking. J Cell Mol Med 2017;21:2514-23.
41. Wegener FT, Ehrlich JR, Hohnloser SH. Dronedarone: an emerging agent with rhythm- and rate-controlling effects. J Cardiovasc Electrophysiol 2006;17 Suppl 2:S17-20.
42. Shattock MJ, Park KC, Yang H-Y, Lee AWC, Niederer S, MacLeod KT, et al. Restitution slope is principally determined by steady-state action potential duration. Cardiovasc Res 2017;113:817-28.
43. Park JH, Pak H-N, Choi EJ, Jang JK, Kim SK, Choi DH, et al. The Relationship Between Endocardial Voltage and Regional Volume in Electroanatomical Remodeled Left Atria in Patients with Atrial Fibrillation: Comparison of Three-Dimensional Computed Tomographic Images and Voltage Mapping. J Cardiovasc Electrophysiol 2009;20:1349-56.
44. Kowey PR. Pharmacological Effects of Antiarrhythmic Drugs: Review and Update. Arch Intern Med 1998;158:325-32.
45. Khan R. Identifying and understanding the role of pulmonary vein activity in atrial fibrillation. Cardiovasc Res 2004;64:387-94.
46. Sherif HM. The developing pulmonary veins and left atrium: implications for ablation strategy for atrial fibrillation. Eur J Cardiothorac Surg 2013;44:792-9.
47. Wang J, Klysik E, Sood S, Johnson RL, Wehrens XHT, Martin JF. Pitx2 prevents susceptibility to atrial arrhythmias by inhibiting left-sided pacemaker specification. Proc Natl Acad Sci U S A 2010;107:9753-8.
48. Chen SA, Hsieh MH, Tai CT, Tsai CF, Prakash VS, Yu WC, et al. Initiation of atrial fibrillation by ectopic beats originating from the pulmonary veins: electrophysiological characteristics, pharmacological responses, and effects of radiofrequency ablation. Circulation 1999;100:1879-86.
49. Saad MN, Morin DP, Khatib S. Atrial fibrillation: current perspective. The Ochsner journal 2009;9:241-7.
50. Narayan SM, Jalife J. CrossTalk proposal: Rotors have been demonstrated to drive human atrial fibrillation. The Journal of physiology 2014;592:3163-6.
51. Chen J, Mandapati R, Berenfeld O, Skanes AC, Gray RA, Jalife J. Dynamics of wavelets and their role in atrial fibrillation in the isolated sheep heart. Cardiovasc Res 2000;48:220-32.
52. Hwang M, Song J-S, Lee Y-S, Li C, Shim EB, Pak H-N. Electrophysiological Rotor Ablation in In-Silico Modeling of Atrial Fibrillation: Comparisons with Dominant Frequency, Shannon Entropy, and Phase Singularity. PLOS ONE 2016;11:e0149695.
53. Kalifa J, Tanaka K, Zaitsev AV, Warren M, Vaidyanathan R, Auerbach D, et al. Mechanisms of Wave Fractionation at Boundaries of High-Frequency Excitation in the Posterior Left Atrium of the Isolated Sheep Heart During

Atrial Fibrillation. Circulation 2006;113:626-33.
54. Wu T-J, Lin S-F, Weiss JN, Ting C-T, Chen P-S. Two Types of Ventricular Fibrillation in Isolated Rabbit Hearts. Circulation 2002;106:1859-66.
55. Pandit SV, Berenfeld O, Anumonwo JM, Zaritski RM, Kneller J, Nattel S, et al. Ionic determinants of functional reentry in a 2-D model of human atrial cells during simulated chronic atrial fibrillation. Biophys J 2005;88:3806-21.
56. Sánchez C, Corrias A, Bueno-Orovio A, Davies M, Swinton J, Jacobson I, et al. The Na+/K+ pump is an important modulator of refractoriness and rotor dynamics in human atrial tissue. Am J Physiol Heart Circ Physiol 2012;302:H1146-59.
57. Prakosa A, Arevalo HJ, Deng D, Boyle PM, Nikolov PP, Ashikaga H, et al. Personalized virtual-heart technology for guiding the ablation of infarct-related ventricular tachycardia. Nat Biomed Eng 2018;2:732-40.
58. Nygren A, Fiset C, Firek L, Clark JW, Lindblad DS, Clark RB, et al. Mathematical Model of an Adult Human Atrial Cell. Circ Res 1998;82:63-81.
59. Maleckar MM, Greenstein JL, Giles WR, Trayanova NA. K+ current changes account for the rate dependence of the action potential in the human atrial myocyte. American Journal of Physiology-Heart and Circulatory Physiology 2009;297:H1398-H410.
60. Koivumäki JT, Korhonen T, Tavi P. Impact of Sarcoplasmic Reticulum Calcium Release on Calcium Dynamics and Action Potential Morphology in Human Atrial Myocytes: A Computational Study. PLoS Comput Biol 2011;7:e1001067.
61. Lopez-Perez A, Sebastian R, Ferrero JM. Three-dimensional cardiac computational modelling: methods, features and applications. Biomed Eng Online 2015;14:35.

ABSTRACT (IN KOREAN)

항부정맥제 사용 후 심방세동 파동의 공간적 변화: 전산 모델링 연구

<지도교수 박 희 남>

연세대학교 대학원 의과학과

황 인 석

배경 우리는 이전에 심방세동 (AF) 환자에서 다중 AAD를 평가하기 위해 컴퓨터 모델링 유도 항부정맥제 (AAD) 테스트가 가능하다고 보고함. 우리는 AADs의 anti-AF 메커니즘과 AF 파동 역학의 공간적 변화를 현실적인 계산 모델을 통해 탐구함.

방법 우리는 5가지 AAD (아미오다론, 소탈롤, 드로네다론, 플레카이니드 및 프로파페논)의 효과를 특성화 하기 위해 좌심방 (LA)의 해부학, 조직학 및 전기 생리학을 반영하는 25명의 AF 환자 (68% 남성, 59.8±9.8세, 32.0% 발작성 AF)의 실제 계산 모델링을 사용함. 우리는 LA의 10개 부분에서 평균 지배 주파수(DF)와 변동 계수 (DF-COV)를 측정하여 AF 파동 역학의 공간적 변화를 평가함. 평균 DF와 DF-COV는 폐정맥(PV) 대 extra-PV, 복원 곡선의 최대 기울기 (Smax) 및 AF의 조각 모음에 따라 비교함.

결과 평균 DF는 용량 의존 방식으로 AAD 투여 후 감소함($p<0.001$). AADs 하에서, DF는 extra-PV 영역보다 PV에서 유의하게 낮았고 ($p<0.001$) COV-DF는 더 높았다($p=0.003$). 평균DF는 AAD에서 낮은 Smax 조건보다 높은 Smax(≥1.4)에서 상당히 낮았음. AF 조각 모음 에피소드 동안 평균 DF는 조각 모음이 없는 경우보다 낮았지만 ($p<0.001$) COV-DF는 더 높았음 ($p<0.001$).

결론 AAD를 사용한 DF 감소는 PV 및 높은 Smax 조건에서 우세하며 낮은 DF 및 공간적으로 불안정한 (높은 DF-COV) 조건에서 AF 종료

또는 조각 모음을 유발함.

핵심 되는 말 : 심방세동, 전산모델링, 항부정맥제, 우세주파수, 공간변화